ChemPubSoc Europe

DOI: 10.1002/chem.201405312

CHEMISTRY
A European Journal
Full Paper

Microalgae Oil

Impact of the Oxygen Defects and the Hydrogen Concentration on the Surface of Tetragonal and Monoclinic ZrO_2 on the Reduction Rates of Stearic Acid on Ni/ZrO_2

Sebastian Foraita,[a] John L. Fulton,[b] Zizwe A. Chase,[b] Aleksei Vjunov,[b] Pinghong Xu,[c] Eszter Baráth,[a] Donald M. Camaioni,[b] Chen Zhao,[a] and Johannes A. Lercher*[a, b]

Abstract: The role of the specific physicochemical properties of ZrO_2 phases on Ni/ZrO_2 has been explored with respect to the reduction of stearic acid. Conversion on pure *m*-ZrO_2 is 1.3 times more active than on *t*-ZrO_2, whereas Ni/m-ZrO_2 is three times more active than Ni/t-ZrO_2. Although the hydrodeoxygenation of stearic acid can be catalyzed solely by Ni, the synergistic interaction between Ni and the ZrO_2 support causes the variations in the reaction rates. Adsorption of the carboxylic acid group on an oxygen vacancy of ZrO_2 and the abstraction of the α-hydrogen atom with the elimination of the oxygen atom to produce a ketene is the key to enhance the overall rate. The hydrogenated intermediate 1-octadecanol is in turn decarbonylated to heptadecane with identical rates on all catalysts. Decarbonylation of 1-octadecanol is concluded to be limited by the competitive adsorption of reactants and intermediate. The substantially higher adsorption of propionic acid demonstrated by IR spectroscopy and the higher reactivity to O_2 exchange reactions with the more active catalyst indicate that the higher concentration of active oxygen defects on *m*-ZrO_2 compared to *t*-ZrO_2 causes the higher activity of Ni/m-ZrO_2.

Introduction

Microalgae are seen as ideal basis for third-generation biofuels, because of their high growth rates and their oil contents as well as the independence of fresh water and arable lands.[1] Their high content of triglycerides makes them a promising resource for liquid transportation fuels. The traditional hydrotreating by using sulfided $NiMo/Al_2O_3$ catalysts has been commercially realized, that is, the NExBTL process (Neste Oil, Porvoo, 340 kt a^{-1}).[2] Although the process for hydrotreating of triglycerides can use the existing infrastructure and requires moderate capital investment, the sulfide catalysts are not ideal for the conversion of a nearly sulfur-free triglyceride feedstock, because they deactivate through sulfur elimination and contaminate the product stream with organic sulfides.[3]

As sulfur-free supported metal catalysts would be attractive alternatives, we have developed two types of novel Ni-based catalysts to directly convert crude microalgae oil quantitatively to diesel-range hydrocarbons under mild conditions of 260 °C and 40 bar H_2.[4] The catalysts used are stable, economic, and scalable. The conversion of the representative model compound stearic acid on Ni/ZrO_2 in presence of H_2 shows that it undergoes reduction of the fatty acid solely by Ni and synergistically by Ni and the ZrO_2 support. In the presence of Ni the acid is hydrogenated to the aldehyde, followed by decarbonylation of the aldehyde to an alkane. The oxygen vacancies of the ZrO_2 support facilitate the concerted adsorption of fatty acid and the activation of H_2. The α-H abstraction and elimination of H_2O lead to a ketene that is formed as a relatively stable intermediate, which has been directly monitored by in-situ IR spectroscopy.[5] In the following step, the ketene is hydrogenated to the corresponding aldehyde, which is in turn hydrodeoxygenated to the corresponding alkane through decarbonylation. The redundancy of the two catalytic sites increases the overall rate.

The best results are obtained by combining an appropriate concentration of the oxygen defect sites with the metal providing the required dissociated hydrogen. It should be noted in passing that much higher rates of the hydrogenation of CO to methanol were observed for Cu/m-ZrO_2 than for Cu/t-ZrO_2,[6] the higher apparent first order-rate constant for Cu/m-ZrO_2 than for Cu/t-ZrO_2 being attributed to the higher concentration

[a] S. Foraita, Dr. E. Baráth, Dr. C. Zhao, Prof. Dr. J. A. Lercher
Department of Chemistry and Catalysis Research Center
Technische Universität München
Lichtenbergstr. 4, 85747 Garching (Germany)
E-mail: johannes.lercher@ch.tum.de

[b] Dr. J. L. Fulton, Z. A. Chase, A. Vjunov, Dr. D. M. Camaioni, Prof. Dr. J. A. Lercher
Institute for Integrated Catalysis
Pacific Northwest National Laboratory
902 Battelle Boulevard, Richland, WA 99352 (USA)

[c] P. Xu
Department of Chemical Engineering and Materials Science
University of California, Davis
1 Shields Avenue, Davis, CA 95616 (USA)

Supporting information for this article is available on the WWW under http://dx.doi.org/10.1002/chem.201405312.

© 2014 Wiley-VCH Verlag GmbH & Co. KGaA, Weinheim

of hydrogen on the surface of *m*-ZrO_2. The difference in the properties of the lattice oxygen of the two ZrO_2 phases was speculated to be related to the specific adsorption properties for hydrogen and CO. As the properties of oxygen vacancies of the supports are critical elements for the hydrodeoxygenation of fatty acids, we decided to explore the effect of *m*-, *t*-, and *mix*-phases of ZrO_2 on the hydrodeoxygenation of stearic acid and 1-octadecanol in the liquid phase. The relation between the physicochemical properties of the support, as well as its influence on the properties of the supported Ni particles for the catalytic activity and the selectivity are explored in the quest to find more active and selective catalysts for fuel synthesis from biomass.

Results and Discussion

Catalyst characterization

The two phases of *m*- and *t*-ZrO_2 were synthesized by the solvothermal method by using water and methanol as solvents, respectively. The XRD patterns for the three ZrO_2 supports are displayed in the Supporting Information. The diffractogram of monoclinic ZrO_2 showed the typical characteristic 2θ reflections at 24.5, 28.3, 31.6, and 34.5° (JCPDS card No. 37-1484). The crystal phase of pure *t*-ZrO_2 was confirmed by XRD diffraction peaks at 2θ of 30.4 and 35.1° (JCPDS card No. 17-0923), without peaks from *m*-ZrO_2. Mixed-phase ZrO_2 from calcination of $Zr(OH)_4$ showed both, characteristic reflections from *m*- and *t*-ZrO_2, and the specific sample consisted of 83% monoclinic and 17% tetragonal phase as derived from Equation (6) (see the Experimental Section).

The N_2 sorption showed that the specific Brunauer–Emmett–Teller (BET) surface areas of the three ZrO_2 supports varied between 117 and 160 $m^2 g^{-1}$ (Table 1). After Ni incorporation and further thermal treatment by calcination and reduction, the specific BET surface areas decreased to approximately 70 $m^2 g^{-1}$ for the three Ni/ZrO_2 catalysts (Table 2). The concentration of acid and base sites of the parent ZrO_2 and Ni/ZrO_2 were determined from the temperature-programmed desorption (TPD) of NH_3 and CO_2, respectively. The concentrations of Lewis acid and base sites of the three ZrO_2 supports were almost identical at 0.30 and 0.04 mmol g^{-1}, respectively. Normalized to the specific surface areas, the Lewis acidity and basicity of the supports were 2.0 and 0.3 μmol m^{-2}, respectively, which demonstrates that the acid and base properties are very similar. With Ni deposited, the acid site concentrations of the three Ni/ZrO_2 samples decreased by 50% to 0.11–0.14 mmol g^{-1}, whereas the concentrations of base sites were almost unchanged (0.04 mmol g^{-1}). This suggests that deposited Ni (metal, oxide, or hydroxide) particles interact with and block Lewis acid sites. The surface areas as well as the concentration and strength of the acid and base sites for the three ZrO_2 and Ni/ZrO_2 samples are shown to be very similar; therefore, the influence from these factors is expected to be minimal.

Table 1. Physicochemical properties of the ZrO_2 supports.

Support	S_{BET} [$m^2 g^{-1}$]	Acid site concentration[a] [mmol g^{-1}]	[μmol m^{-2}]	Basic site concentration[b] [mmol g^{-1}]	[μmol m^{-2}]
mix-ZrO_2	162	0.33	2.0	0.06	0.37
m-ZrO_2	117	0.30	2.5	0.04	0.36
t-ZrO_2	149	0.30	1.9	0.04	0.27

[a] Determined by TPD of NH_3. [b] Determined by TPD of CO_2.

Table 2. Physicochemical properties of the Ni-incorporated ZrO_2 catalysts.

Catalyst	Ni loading [wt%]	S_{BET} [$m^2 g^{-1}$]	$d_{Ni(111)}$[c] [nm]	Acid site concentration[a] [mmol g^{-1}]	[mol m^{-2}]	Basic site concentration[b] [mmol g^{-1}]	[mol m^{-2}]
Ni/*mix*-ZrO_2	9.7	75	12	0.14	1.8	0.05	0.69
Ni/*m*-ZrO_2	9.7	69	13	0.11	1.6	0.04	0.58
Ni/*t*-ZrO_2	10	70	12	0.11	1.5	0.04	0.54

[a] Determined by TPD of NH_3. [b] Determined by TPD of CO_2. [c] Calculated from XRD by using the Scherrer equation.

The characteristic diffraction peaks for *m*- and *t*-ZrO_2 for the three Ni/ZrO_2 (Figure S1 B, in the Supporting Information) samples were in good agreement with the diffractogram of the parent supports (Figure S1 A in the Supporting Information), suggesting that the synthesized phases are very stable against phase transformation during impregnation, calcination, and reduction. The distinctive peaks at 2θ of 44.6 and 51.9° are assigned to Ni(111) and Ni(200), respectively. Based on the Scherrer equation, the average particle diameter, $d_{Ni(111)}$, of Ni/*mix*-ZrO_2, Ni/*m*-ZrO_2, and Ni/*t*-ZrO_2 were 12, 13, and 12 nm, respectively.

Apart from XRD measurement on determining the Ni particle size, TEM images with energy-dispersive X-ray spectroscopy (EDX) mapping of Ni on ZrO_2 (Figure 1 A) and the corresponding particle-size distributions (Figure 1 B) are also shown. Note that the TEM images of ZrO_2-supported Ni particles are difficult to interpret because of the low metal/support contrast.[7] Therefore, element-sensitive EDX-technique was applied to differentiate between the metal species and the support. It shows Ni particles in contact with ZrO_2. From the TEM micrographs spherically shaped Ni particles with a heterogeneous size distribution, typically for wetness impregnation technique, and an average diameter of 14–15 nm were detected, that is, larger in size than the average size determined from XRD. This is attributed to the fact that TEM counts the size of visible Ni^0 particles, whereas XRD accounts also for particles with too low contrast to be determined by TEM measures.[8] Generally, Ni particles show comparable sizes and distributions and shapes on three ZrO_2 supports determined from both XRD patterns and TEM images.

The state of Ni on ZrO_2 was probed by temperature-programmed reaction (TPR) of three calcined Ni/ZrO_2 catalysts by

© 2014 Wiley-VCH Verlag GmbH & Co. KGaA, Weinheim

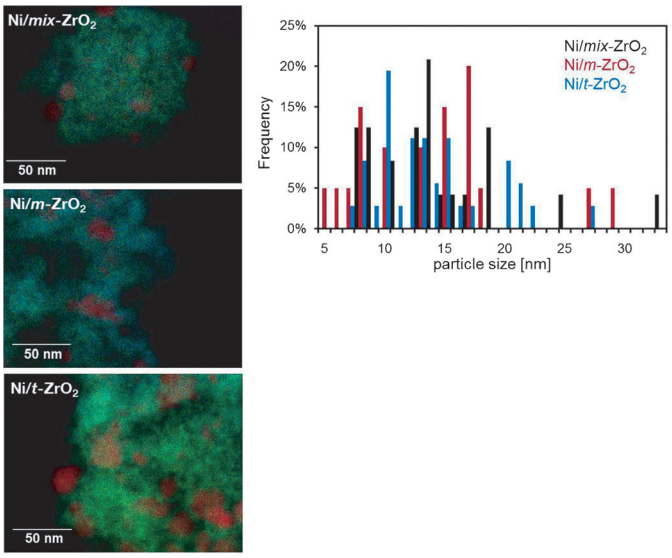

Figure 1. a) TEM images with recorded by using energy-dispersive X-ray spectroscopy (EDX) mapping (Ni in red, Zr in green, and O in blue) and b) the corresponding Ni particle-size distribution of the three Ni/ZrO_2 catalysts.

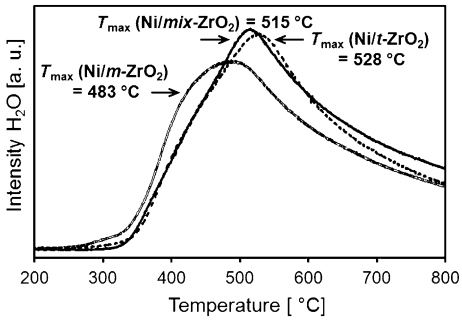

Figure 2. Temperature-programmed reduction with H_2 on Ni/*mix*-ZrO_2, Ni/*m*-ZrO_2, and Ni/*t*-ZrO_2.

using H_2 (see Figure 2). The TPR showed that the maximum rates of reduction (monitored by H_2O formation) appeared between 483 and 528 °C. The maximum reduction rate for Ni/*m*-ZrO_2 occurred at 483 °C, whereas for Ni/*mix*-ZrO_2 and Ni/*t*-ZrO_2, the reduction rates peaked at somewhat higher temperatures, that is, 515 and 528 °C, respectively. Bulk NiO is usually reduced at 400 °C,[9] and the higher temperature observed here is tentatively attributed to the reduction of small nickel oxide crystallites interacting strongly with ZrO_2.[8] Reducing the three calcined Ni/ZrO_2 catalysts at 500, 550, and 600 °C showed that the Ni particles gradually grew as a function of the reduction temperature, leading to particles with 13, 14, and 19 nm diameter, respectively (determined by the Scherrer equation from the XRD patterns, see Table S1 in the Supporting Information). The catalytic activities for the hydrogenation of stearic acid decreased in the order of 2.6, 2.0, and 1.0 mmol g^{-1} h^{-1}, indicating that the specific rates of hydrogenation decreased in accordance with the increasing size of the Ni particles. To achieve a high hydrodeoxygenation rate, the calcined Ni/ZrO_2 sample were reduced at 500 °C for all samples discussed here.

States of Ni and the ZrO_2 polymorphic phases by XAFS

The states of Ni and Zr in the three different Ni/ZrO_2 catalysts are analyzed by Ni and Zr K-edge XAFS. The Ni K-edge XANES spectra demonstrate that the three Ni/*m*-ZrO_2, Ni/*t*-ZrO_2, and Ni/*mix*-ZrO_2 catalysts contained a higher concentration of Ni^0 than Ni^{II} (Figure 3 A). The Fourier-transformed Ni K-edge EXAFS

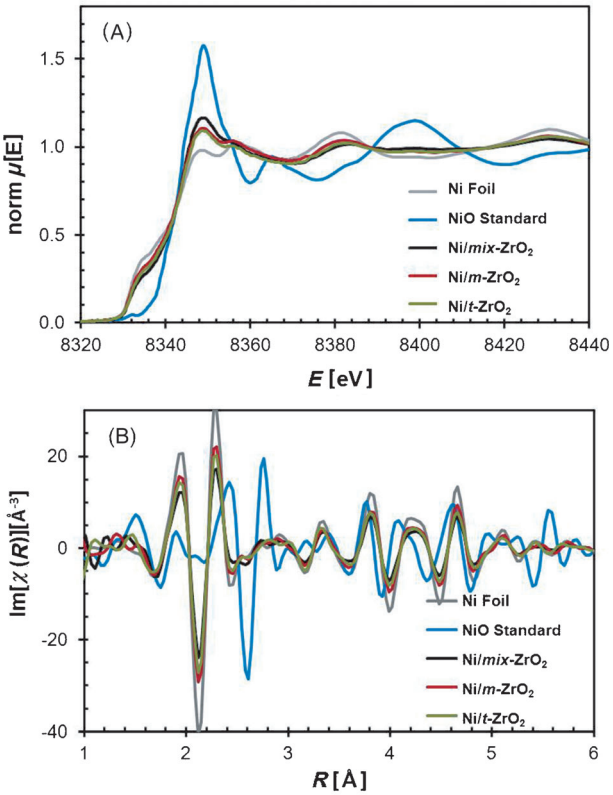

Figure 3. A) Ni K-edge XANES spectra and B) Ni K-edge EXAFS spectra Fourier-transformed (FTs) Im[$\chi(R)$] spectra of the Ni standards (Ni^0 foil, NiO) and the Ni/ZrO_2 catalysts (Ni/*mix*-ZrO_2, Ni/*m*-ZrO_2, and Ni/*t*-ZrO_2) at ambient temperature.

spectra were quite similar for the three Ni/ZrO_2 catalysts, which is in good agreement with the other results discussed. The fractions of Ni^0 and Ni^{II}, analyzed by a linear combination from XANES, are compiled in Table S2 in the Supporting Information. The three Ni/ZrO_2 catalysts contained approximately 70–79% metallic Ni^0 and 21–30% Ni^{II} before reaction. The Ni–Ni distances and the coordination numbers (Figure 3 B) are identical to that of bulk Ni. After reaction in presence of H_2, the fraction of metallic Ni^0 increased to 84–86%. Fitting the EXAFS by using a theoretical standard (Figure S4 in the Supporting Information) showed that also for these experiments the coordination number of the first Ni–Ni shell was identical to that for the bulk metal. This is consistent with Ni nanoparticle diameters that are greater than about 5 nm as shown also by TEM (Figure 1 B). No indication of Ni–Zr scattering, that would be present as a result of a separate, atomically dispersed Ni phase, was observed. The Ni EXAFS structure for Ni/

© 2014 Wiley-VCH Verlag GmbH & Co. KGaA, Weinheim

m-ZrO_2 and for Ni/*t*-ZrO_2 were nearly identical up to $R = 8$ Å and hence the observed higher reactivity of Ni/*m*-ZrO_2 (described below) does not appear to be related to differences in the Ni nanostructures.

The XAS of the Zr K-edge of the three ZrO_2 catalysts (Figure 4A) shows that the XANES of *mix*-ZrO_2, *m*-ZrO_2, and *t*-ZrO_2

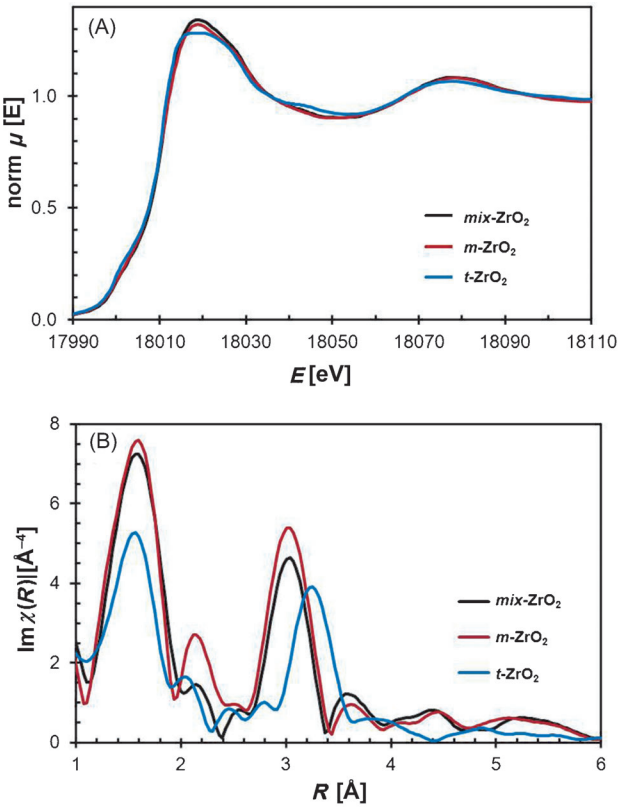

Figure 4. A) Zr K-edge XANES spectra and B) Zr K-edge EXAFS spectra Fourier-transformed (FTs) Im[$\chi(R)$] spectra of *mix*-ZrO_2, *m*-ZrO_2, and *t*-ZrO_2 at ambient temperature.

indicate profound differences for *t*-ZrO_2 in comparison to *m*-ZrO_2 including the stronger 1s→4d shoulder at 18000 eV, the apparent white line doublet at 18020 eV, and the scattering peak at 18045 eV. A more subtle feature is the shoulder on the leading edge of the white line at 18015 eV, which appeared also for the pure *t*-ZrO_2. All features are consistent with published values of ZrO_2.[10] By using the XANES data to differentiate *t*-ZrO_2 and *m*-ZrO_2, a linear combination fit to the *mix*-ZrO_2 yields a ratio of 25% of *t*-ZrO_2 and 75% of *m*-ZrO_2 (Table S3 in the Supporting Information), which is in good agreement with the XRD results in Figure S1 in the Supporting Information. After deposition of Ni, the structure of ZrO_2 was hardly changed (see Figure S5 in the Supporting Information). Calcination and reduction steps, however, alter the ZrO_2 phase distribution of *t*-ZrO_2 and *mix*-ZrO_2. In both instances *t*-ZrO_2 is partially converted to the *m*-ZrO_2 phase. The *t*-ZrO_2 phase is converted to about 38% *m*-ZrO_2, whereas *mix*-ZrO_2 is converted to about 94% to *m*-ZrO_2.

In line with the XRD patterns, the Fourier-transformed Zr EXAFS spectra (Figure 4B) showed high similarity between *mix*-ZrO_2 and *m*-ZrO_2. The first maximum at 1.5 Å is assigned to the nearest shell (O), whereas the second peak at 3.0–3.3 Å is attributed to the next nearest shell (Zr) around the Zr central atom.[11] The shift of the peak at 3.3 Å for *t*-ZrO_2 (compared to 3.0 Å for *m*-ZrO_2) in the FT imaginary $\chi(R)$ plot (Figure 4B) is attributed to the fact that the Zr–O bond length is different in *m*-ZrO_2 ($Zr–O_I$, trigonal and $Zr–O_{II}$, tetrahedral) and *t*-ZrO_2 ($Zr–O_{II}$, tetrahedral)..[12] This peak shift from 3.3 to 3.0 Å is also related to a decreasing symmetry as varying from the tetragonal to the monoclinic phase.[11a]

Hydrogenation of stearic acid over ZrO_2

To investigate the effect of the ZrO_2 morphologies, stearic acid was converted first on the bare supports. The three supports led to similar distributions of the products after 6 h (see Figure 5). The major products were the aldehyde (selectivity: 60–75%) and the diheptadecyl ketone (selectivity: 18–27%), as well as small concentrations of the heptadecane (selectivity: 6–13%).

The reduction and ketonization of the carboxylic acid has been reported to be catalyzed by modestly redox-active oxides such as ZrO_2, CeO_2, Cr_2O_3, Fe_2O_3, ZnO, and TiO_2 at 300–

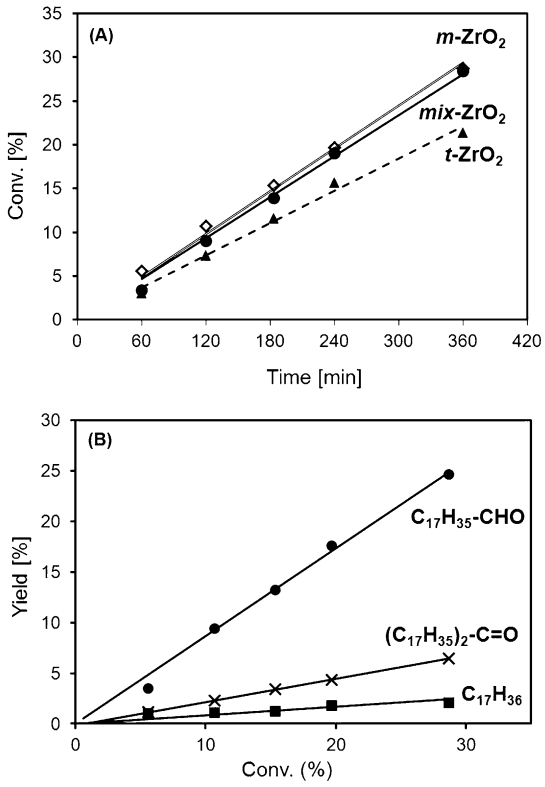

Figure 5. A) Conversion of stearic acid over *m*-ZrO_2, *mix*-ZrO_2, and *t*-ZrO_2 as a function of time. B) Yields of octadecanal, diheptadecyl ketone, and *n*-heptadecane over *m*-ZrO_2 as a function of the conversion of stearic acid. Reaction conditions: stearic acid (0.5 g), ZrO_2 (0.5 g), dodecane (100 mL), 260 °C, $p(H_2) = 40$ bar, stirring at 600 rpm. Reproducibility of the rates has been better than ±5%.

© 2014 Wiley-VCH Verlag GmbH & Co. KGaA, Weinheim

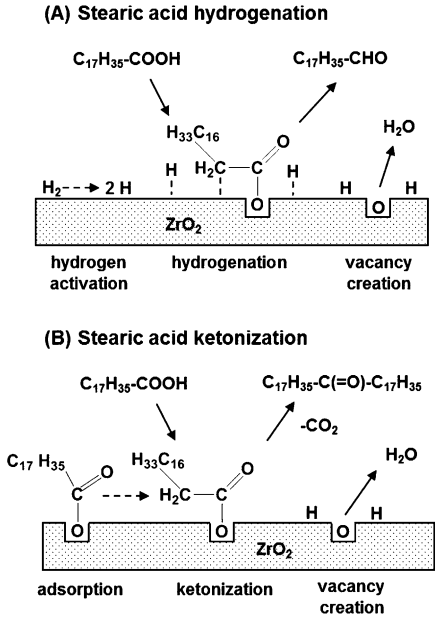

Scheme 1. Mechanisms for A) the hydrogenation and B) the ketonization of stearic acid on the surface of ZrO_2.

400 °C.[13] The catalyzed reaction involves the adsorption of the acid on the oxygen defect sites of the metal oxides to form a carboxylate. The carboxylates are assumed to be adsorbed parallel to the oxide surface because of the strong interaction of the α-H atoms with the surface. Ketene and H_2O are formed through abstraction of one of the α-H atoms. Subsequently, a nearby carboxylate reacts with the activated hydrogen atoms (Scheme 1 A) to form the aldehyde or with the adsorbed ketene to form the ketone by eliminating CO_2 (Scheme 1 B).

The rates of the conversion of stearic acid on *mix*- and *m*-ZrO_2 were similar at 28 and 29% after 6 h corresponding to rates of 0.017 and 0.016 mmol $g^{-1} h^{-1}$, respectively. The rate on *t*-ZrO_2 was 20% lower (Table 3). The *mix*-ZrO_2 consisted of a majority of 83% *m*-ZrO_2 evidenced by the XRD patterns. This demonstrates that the monoclinic phase of ZrO_2 is more active for the reduction of stearic acid even in the absence of metal sites.

Hydrogenation of stearic acid with Ni/ZrO_2

The results of the conversion of stearic acid on the Ni supported on the *m*-, *t*-, and *mix*-ZrO_2 phases are shown in Figure S6 A in the Supporting Information. The primary initial product was the hydrogenated alcohol with a selectivity of 86–94%, and further the decarbonylated C_{17} and the hydrodeoxygenated C_{18} hydrocarbons were obtained in minor quantities (total selectivity of 5–10%) (Figure S6 B in the Supporting Information). With Ni/ZrO_2 ketonization was eliminated. In addition, the hydrogenation rate on Ni/*m*-ZrO_2 (2.6 mmol $g^{-1} h^{-1}$) was two orders of magnitude higher than that on *m*-ZrO_2 (0.017 mmol $g^{-1} h^{-1}$). This is attributed to the fact that Ni aided the dissociation of H_2, thereby dramatically enhancing the rate of formation and consequently increasing the number of oxygen vacancies on the ZrO_2 support, thereby substantially increasing the rate of ketene formation by the support. In addition, in the presence of H_2, the direct Ni-catalyzed hydrogenation of stearic acid dominates the overall catalytic chemistry. The facile availability of hydrogen atoms essentially eliminates the much slower ketonization route.

Comparison of the three different Ni/ZrO_2 catalysts shows that the rate of conversion of stearic acid over Ni/*m*-ZrO_2 (2.6 mmol $g^{-1} h^{-1}$) was almost three times higher than that over Ni/*t*-ZrO_2 (0.9 mmol $g^{-1} h^{-1}$) (Table 4). The catalytic activities of Ni/*mix*-ZrO_2 and Ni/*m*-ZrO_2 for producing 1-octadecanol were quite similar with rates of 2.5 and 2.6 mmol $g^{-1} h^{-1}$, respectively. To further verify such a phase effect, Ni supported on a physical mixtures of *m*-ZrO_2 and *t*-ZrO_2 (see Figure S6 A in the Supporting Information) were used to reduce stearic acid under otherwise identical conditions. The hydrogenation rates followed the sequence of 1.7, 1.5, and 1.0 mmol $g^{-1} h^{-1}$ for the 1:2, 1:1, and 2:1 ratios of the Ni/(*m*-ZrO_2/*t*-ZrO_2) samples (see Table 4). The rates with the physically mixed supports were expectedly between the rates of pure Ni/*m*-ZrO_2 (2.6 mmol $g^{-1} h^{-1}$) and Ni/*t*-ZrO_2 samples (0.9 mmol $g^{-1} h^{-1}$). These results show that the rate of reduction is directly correlated with the concentration of *m*-ZrO_2 (Figure 6).

Table 3. Comparison of the conversion of stearic acid over the different ZrO_2 supports.[a]

Catalyst	Rate [mmol $g^{-1} h^{-1}$]	Conversion [%]	Selectivity [C%] C_{17}	C_{17}–CHO	$(C_{17}H_{35})_2C{=}O$
mix-ZrO_2	0.017	28	13	60	27
m-ZrO_2	0.016	29	6.9	75	18
t-ZrO_2	0.013	21	6.0	72	22

[a] Reaction conditions: stearic acid (0.5 g), ZrO_2 (0.5 g), dodecane (100 mL), 260 °C, $p(H_2) = 40$ bar, 6 h, stirring at 600 rpm. Reproducibility of the rates has been better than ±5%.

Table 4. Comparison of the conversion of stearic acid over the different Ni/ZrO_2 catalysts.[a]

Catalyst	Rate [mmol $g^{-1} h^{-1}$]	Conversion [%]	Selectivity [C%] C_{17}	C_{18}	C_{18}–OH
Ni/*mix*-ZrO_2	2.5	13.3	5.5	0.4	94
Ni/*m*-ZrO_2	2.6	12.7	6.3	0.5	93
Ni/*m*-ZrO_2/*t*-ZrO_2 (2:1)	1.7	7.1	11	2.0	87
Ni/*m*-ZrO_2/*t*-ZrO_2 (1:1)	1.5	7.3	9.4	1.6	89
Ni/*m*-ZrO_2/*t*-ZrO_2 (1:2)	1.0	4.4	12	2.0	86
Ni/*t*-ZrO_2	0.9	4.1	7.8	0.2	92

[a] Reaction conditions: stearic acid (1.0 g), Ni/ZrO_2 (10 wt%, 0.10 g), dodecane (100 mL), 260 °C, $p(H_2) = 40$ bar, 2 h, stirring at 600 rpm. Reproducibility of the rates has been better than ±5%.

Decarbonylation of 1-octadecanol over Ni/ZrO_2

The hydrodeoxygenation of stearic acid on Ni/ZrO_2 proceeded with the hydrogenation to 1-octadecanol as the apparent primary product (see Figure S6 in the Supporting Information). To better understand the kinetic sequence, the conversion of 1-

© 2014 Wiley-VCH Verlag GmbH & Co. KGaA, Weinheim

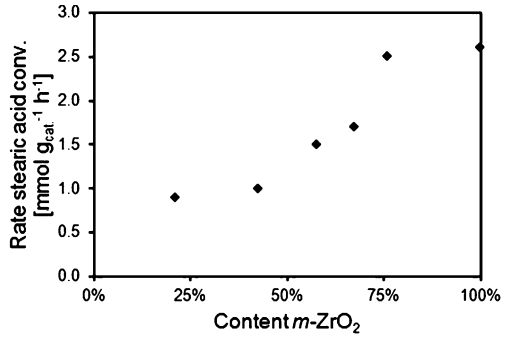

Figure 6. Rates for the conversion of stearic acid depending on the content of monoclinic ZrO_2 in the Ni/ZrO_2 catalyst. Reaction conditions: stearic acid (1.0 g), Ni/ZrO_2 (10 wt%, 0.1 g), dodecane (100 mL), 260 °C, $p(H_2)=40$ bar, stirring at 600 rpm.

octadecanol was studied in separate experiments (Figure 7). A selectivity of 95% for the C_{17} heptadecane and of 5% for octadecane were observed at 36% conversion after 2 h for all samples. This shows that direct decarbonylation (−CO) of the aldehyde, formed through the dehydrogenation of the alcohol took place. The minor concentration of octadecane is concluded to be catalyzed by the sequential dehydration–hydrogenation of the alcohol on acid sites of Ni/ZrO_2. The rate of decarbonylation of octadecanol (6.3 mmol g^{-1} h^{-1}) was identical on all Ni/ZrO_2 catalysts (Figure 7 and Table 5), and such rate was

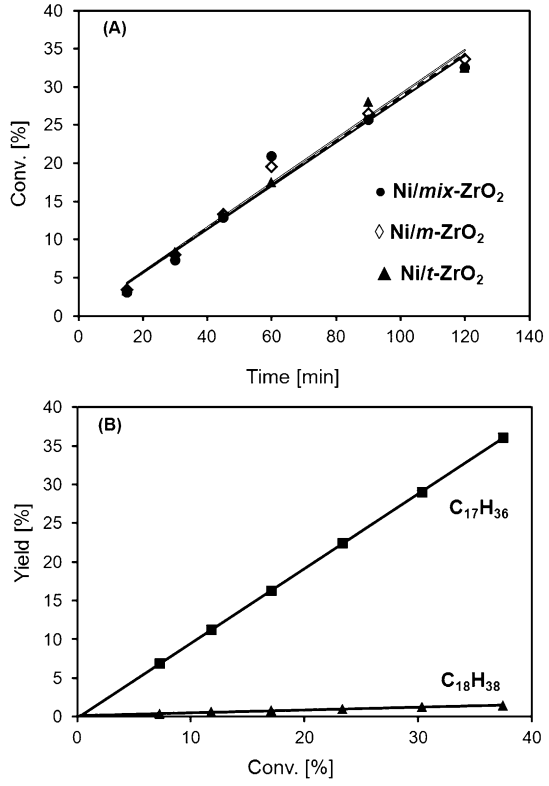

Figure 7. A) Conversion of 1-octadecanol as a function of time. B) Yield of *n*-heptadecane and *n*-octadecane over Ni/*m*-ZrO_2 as a function of the conversion of 1-octadecanol. Reaction conditions: 1-octadecanol (1.0 g), Ni/ZrO_2 (10 wt%, 0.10 g), dodecane (100 mL), 260 °C, $p(H_2)=40$ bar, stirring at 600 rpm. Reproducibility of the rates has been better than ±5%.

Table 5. Comparison of the conversion of 1-octadecanol over the three Ni/ZrO_2 catalysts.[a]

Catalyst	Rate [mmol g^{-1} h^{-1}]	Conversion [%]	Selectivity [C%] C_{17}	C_{18}
Ni/*mix*-ZrO_2	6.3	33	95	5.0
Ni/*m*-ZrO_2	6.3	33	96	4.0
Ni/*t*-ZrO_2	6.2	32	97	3.0

[a] Reaction conditions: 1-octadecanol (1.0 g), Ni/ZrO_2 (10 wt%, 0.10 g), dodecane (100 mL), 260 °C, $p(H_2)=40$ bar, 2 h, stirring at 600 rpm. Reproducibility of the rates has been better than ±5%.

three to seven times higher than that of the hydrogenation of stearic acid, that is, 2.6 and 0.9 mmol g^{-1} h^{-1} on the Ni/*m*-ZrO_2 and Ni/*t*-ZrO_2 catalysts, respectively. This suggests that the rate-determining step is related to the reductive deoxygenation of the fatty acid. The result also implies that the decarbonylation of 1-octadecanol is not sensitive with respect to the ZrO_2 phases, and that the active sites of the Ni particles convert 1-octadecanol with identical rates.

Overall hydrodeoxygenation of stearic acid to heptadecane over Ni/ZrO_2

The kinetics of the overall hydrodeoxygenation of stearic acid to heptadecane over Ni/*m*-ZrO_2 and Ni/*t*-ZrO_2 at 260 °C is shown in Figure 8. 1-Octadecanol is the initial product, being formed in yields of 60–80%, although the final product is primarily heptadecane. Octadecanal and 1-octadecanol being in equilibrium through facile Ni-catalyzed hydrogenation/dehydrogenation reactions account for this conversion of 1-octadecanol to heptadecane. At the high H_2 pressure (40 bar), the concentration of the aldehyde is too low to be observed. Nevertheless, the intermediate 1-octadecanal is slowly and irreversibly decarbonylated to heptadecane, effectively converting 1-octadecanol into heptadecane. 1-Octadecanol also underwent esterification with stearic acid to form stearyl stearate (reversible reaction) as well as dehydration/hydrogenation to octadecane as side products. Ni/*m*-ZrO_2 achieved a much higher rate for the reduction of stearic acid forming 1-octadecanol as well as overall hydrodeoxygenation rates for producing heptadecane from stearic acid (see Figure 8), which is fitted with the results from kinetic measurements of the individual steps. A simplified network for the hydrodeoxygenation of stearic acid over the Ni/ZrO_2 catalysts is displayed in Scheme 2. The elementary steps include hydrogenation of stearic acid (A) to 1-octadecanol (B), then 1-octadecanol (B) is decarbonylated to heptadecane (C). In addition, dehydration/hydrogenation of 1-octadecanol (B) forms octadecane without carbon loss, and esterification of stearic acid (A) and 1-octadecanol (B) produces an ester (D). The latter esterification reaction is in equilibrium. The H_2 partial pressure before and after the reaction was 40 bar. Assuming first-order reaction steps, the elementary rate equations are listed as follows [Eqs. (1)–(5)]:

© 2014 Wiley-VCH Verlag GmbH & Co. KGaA, Weinheim

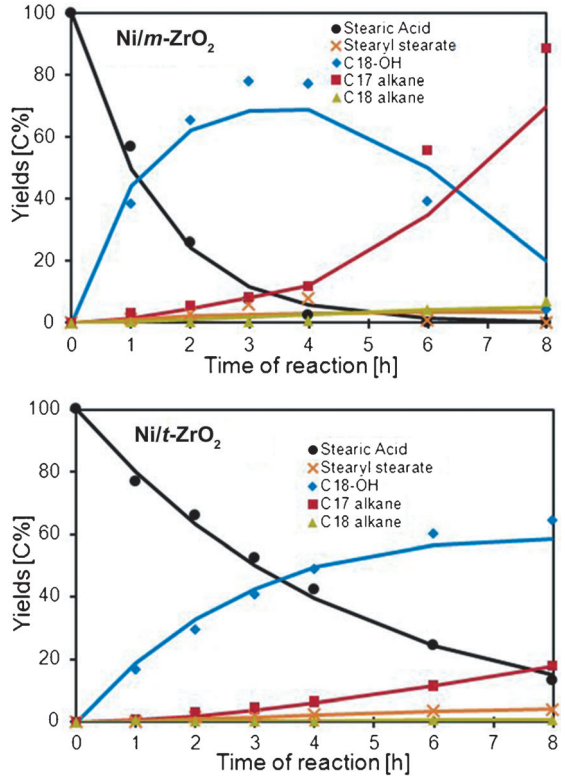

Figure 8. Fitting of the data for the hydrodeoxygenation of stearic acid by using Ni/*m*-ZrO_2 and Ni/*t*-ZrO_2 as a function of time (solid points = experimental data, lines = itted data). Reaction conditions: stearic acid (0.5 g), Ni/ZrO_2 (10 wt%, 0.2 g), dodecane (100 mL), 260 °C, $p(H_2)$ = 40 bar, stirring at 600 rpm.

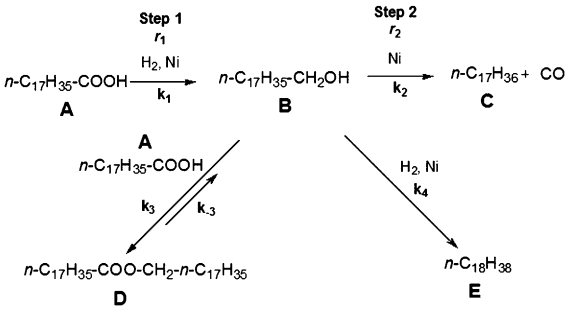

Scheme 2. Proposed elementary steps for the hydrodeoxygenation of stearic acid to C_{17} heptadecane.

$$\frac{dc(A)}{dt} = -k_1 c(A) - k_3 c(A)c(B) + k_{-3} c(D) \quad (1)$$

$$\frac{dc(B)}{dt} = k_1 c(A) - k_2 c(B) - k_3 c(B)c(A) + k_{-3} c(D) - k_4 c(B) \quad (2)$$

$$\frac{dc(C)}{dt} = k_2 c(B) \quad (3)$$

$$\frac{dc(D)}{dt} = k_3 c(A)c(B) - k_{-3} c(D) \quad (4)$$

$$\frac{dc(E)}{dt} = k_4 c(B) \quad (5)$$

The rates [Eqs. (1)–(5)] were numerically integrated and fit by least squares to the kinetic data for the hydrodeoxygenation of stearic acid over Ni/*m*-ZrO_2 and Ni/*t*-ZrO_2 (see Figure 8). The fitted rate constant ($k_1 = 2.7\times10^{-3}$ min^{-1}) for the hydrogenation of stearic acid over Ni/*m*-ZrO_2 was almost identical to the value from the individual reaction step measurement ($k_1 = 2.2\times10^{-3}$ min^{-1}) (see Table 6). However, the reaction rates for the decarbonylation of the alcohol were not consistent between the fitted data ($k_2 = 2.4\times10^{-4}$ min^{-1}) and the calculated individual measurement ($k_2 = 7.5\times10^{-3}$ min^{-1}). The rate constants of the side reactions k_3 for the esterification ($k_3 = 5.0\times10^{-6}$ min^{-1}) as well as k_4 for the dehydration/hydrogenation towards octadecane ($k_4 = 1.2\times10^{-5}$ min^{-1}) were two orders of magnitude lower than k_1 ($k_1 = 2.7\times10^{-3}$ min^{-1}). The substantially lower rate constant k_2 in the fitted overall hydrodeoxygenation is attributed to either competition of stearic acid and 1-octadecanol in the conversion (major part), or to side reactions such as esterification and dehydration of 1-octadecanol (a very minor part). Meanwhile, the apparent esterification rate constant k_3 (5.0×10^{-6} min^{-1}) was five magnitudes higher than its reverse rate k_{-3} (1.9×10^{-11} min^{-1}). Therefore, the forward reaction of the esterification is concluded to be more favored in the tested time period. Note that as 1-octadecanol and stearic acid are consumed continuously along the reaction time, the equilibrium would be shifted to the reverse reaction for the cleavage of the C–O bond of stearyl stearate. Compared to Ni/*m*-ZrO_2 ($k_1 = 2.7\times10^{-3}$ min^{-1}), Ni/*t*-ZrO_2 showed a three times lower hydrogenation rate ($k_1 = 9.2\times10^{-4}$ min^{-1}) for hydrogenation of stearic acid (see Table 6 B), which was identical to the rate comparison in the individual steps measurement (see Table 6 A). The rate of the decarbonylation of 1-octadecanol on Ni/*t*-ZrO_2 ($k_2 = 2.1\times10^{-4}$ min^{-1}) was identical to that on Ni/*m*-ZrO_2 ($k_2 = 2.4\times10^{-4}$ min^{-1}) in the overall hydrodeoxygenation of stearic acid (see Table 6 B), which is in agreement with the rate comparison in the individual measurements ($k_2 = 7.4$ and 7.5×10^{-3} min^{-1}, respectively, see Table 6 A). The lower rate of

Table 6. Rate constants in the individual steps and fitted rate constants in the overall hydrodeoxygenation of stearic acid with Ni/*m*-ZrO_2 and Ni/*t*-ZrO_2 (normalized to conditions: stearic acid 1.0 g, catalyst 0.1 g, 260 °C, $p(H_2)$ = 40 bar, stirring at 600 rpm).

A) Rate constants determined from individual steps

catalyst	step 1: hydrogenation of stearic acid $r_1 = k_1 c(C_{17}H_{35}COOH)$	step 2: decarbonylation of 1-octadecanol $r_2 = k_2 c(C_{17}H_{35}\text{-}CH_2OH)$
Ni/*m*-ZrO_2	$k_1 = 2.2\times10^{-3}$ min^{-1}	$k_2 = 7.5\times10^{-3}$ min^{-1}
Ni/*t*-ZrO_2	$k_1 = 7.9\times10^{-4}$ min^{-1}	$k_2 = 7.4\times10^{-3}$ min^{-1}

B) Fitted rate constants in the overall hydrodeoxygenation of stearic acid

	k_1 [min^{-1}]	k_2 [min^{-1}]	k_3 [min^{-1}]	k_{-3} [min^{-1}]	k_4 [min^{-1}]
Ni/*m*-ZrO_2	2.7×10^{-3}	2.4×10^{-4}	5.0×10^{-6}	1.9×10^{-11}	1.2×10^{-5}
Ni/*t*-ZrO_2	9.2×10^{-4}	2.1×10^{-4}	1.5×10^{-6}	2.9×10^{-11}	8.5×10^{-6}

© 2014 Wiley-VCH Verlag GmbH & Co. KGaA, Weinheim

the decarbonylation of 1-octadecanol in the overall hydrodeoxygenation process compared to the individual steps is majorly attributed to the competition in species adsorption with stearic acid onto the active Ni sites. For the reversible esterification (k_3 and k_{-3}) and the dehydration (k_4) of 1-octadecanol, the rates were comparable on the Ni/*m*-ZrO_2 and Ni/*t*-ZrO_2 catalysts (see Table 6 B) probably because of their similar acidity and basicity. In addition, the rate constants of the side reactions (k_3, k_{-3}, and k_4) were magnitudes lower than the major reaction steps of the hydrogenation of stearic acid (k_1) and the decarbonylation of 1-octadecanol (k_2), implying that the influence of side reactions is minimal compared to the overall hydrodeoxygenation.

The mechanism for the hydrodeoxygenation of stearic acid proceeds through two routes. The first relies on the Ni-catalyzed reductive deoxygenation to octadecanal, which is equilibrated with octadecanol. The aldehyde is in turn decarbonylated on Ni. The second pathway starts with the adsorption of stearic acid on the oxygen vacancies of ZrO_2 to form the carboxylate, and then through deoxygenation to the aldehyde. The reductive deoxygenation on the pure ZrO_2 support is quite low (0.016 mmol g^{-1} h^{-1}) presumably because H_2 dissociation—required to maintain oxygen vacancies through desorption of water—is slow (the HD formation, characteristic for H_2 dissociation was at least 10^2 times faster in the presence of Ni than with ZrO_2 alone). The redundant catalytic pathways of Ni and ZrO_2 generate the appropriate combination enhancing the hydrogenation rate of stearic acid by 150 times (2.6 mmol g^{-1} h^{-1}) compared to *m*-ZrO_2 (0.016 mmol g^{-1} h^{-1}). The rate on Ni/ZrO_2 is much higher than that on other Ni-based catalysts such as Ni/C, Ni/Al_2O_3, and Ni/SiO_2,[5] suggesting a strong support effect. In summary, it can be concluded that the major active sites are the Ni particles. The Ni particles on the *m*- and *t*- ZrO_2 supports have been shown to be almost identical by TEM, XRD, TPR, EXAFS, and XANES, as well as by the rates of the decarbonylation of 1-octadecanol. It should be emphasized at this point that the BET surface areas, the concentrations of acid and base sites on parent *m*- and *t*-ZrO_2 and Ni/ZrO_2 were nearly identical. Therefore, the rate differences of the hydrogenation of stearic acid on Ni/*m*-ZrO_2 and Ni/*t*-ZrO_2 are concluded to be related to differences in the adsorption and/or redox properties. These properties will be explored by spectroscopically characterizing variations in the sorption mode and strength of propionic acid as well as with the temperature-programmed isotopic exchange (^{18}O–^{16}O) of *m*- and *t*-phases of ZrO_2.

Comparison of in-situ IR spectroscopy of adsorbed propionic acid on *m*- and *t*-ZrO_2 in the gas phase

The IR spectra of free propionic acid in the gas phase and adsorbed propionic acid on *m*-ZrO_2 are shown in Figure 9. The absorbance bands at $\tilde{\nu}$ = 3600–3700 cm^{-1} for propionic acid in the gas phase (see Table S4 in the Supporting Information) are ascribed to the O–H stretching vibration of the carboxylic acid group. The C=O vibration of the carboxylic acid group is assigned to the doublet at $\tilde{\nu}$ = 1700 and 1800 cm^{-1} and the C–O vibration to the band at $\tilde{\nu}$ = 1150 cm^{-1}. The C–H stretching vibrations of $-CH_3$ and $-CH_2$ are assigned to the bands at $\tilde{\nu}$ = 2945 and 2986 cm^{-1}, respectively. The in-plane bending vibration of C–H is assigned to the triplet bands between $\tilde{\nu}$ = 1400–1500 cm^{-1} and at $\tilde{\nu}$ = 1080 cm^{-1}. When the carboxylic group of the propionic acid was adsorbed on the ZrO_2 surface, the ν(O–H) disappeared and the C=O vibrations at $\tilde{\nu}$ = 1700–1800 cm^{-1} became indistinguishable. This is a primary indication that propionic acid adsorbs on the catalyst surface as bidentate through the carboxylic group (see Table 7).

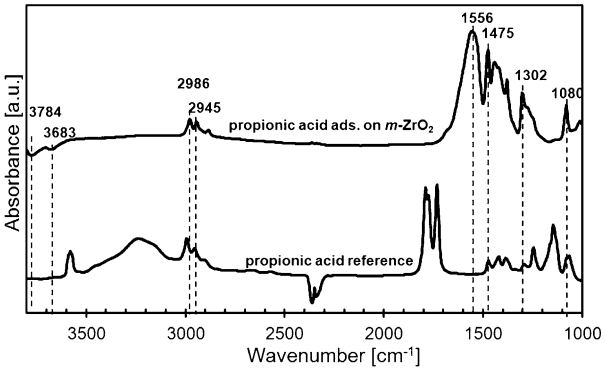

Figure 9. IR spectra of propionic acid (0.05 mbar) adsorbed on *m*-ZrO_2 at 40 °C and of free propionic acid in vapor phase as reference.

Table 7. Adsorbed carboxyl species in the A) bidentate and B) monodentate conformation on the surface of ZrO_2.

A) Symmetric ν_s (left) and anti-symmetric ν_a (right) bidentate stretching vibration of the carboxyl species	B) Monodentate species adsorbed on the catalyst surface
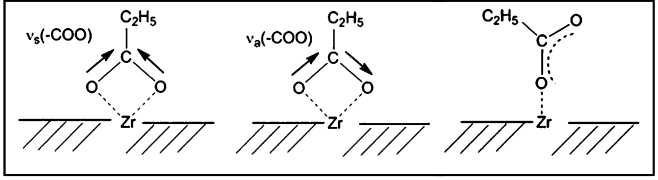	

The bands at $\tilde{\nu}$ = 1556 and 1419 cm^{-1} are attributed to the O–C–O anti-symmetric (ν_a) and symmetric (ν_s) vibrations, respectively (see Table 7 a), which suggest the presence of a symmetric bidentate species with two indistinguishable O atoms. The band at $\tilde{\nu}$ = 1419 cm^{-1} (symmetric ν_s vibrations) may overlap with the more intense δ-CH_3 vibration as part of the C–H triplet ($\tilde{\nu}$ = 1400–1500 cm^{-1}).[13c,d,14] The bands for the C–H vibrations remained unchanged at $\tilde{\nu}$ = 2986 and 2945 cm^{-1} as well as the vibrations of triplet ($\tilde{\nu}$ = 1400–1500 cm^{-1}) and ρ-CH_3 ($\tilde{\nu}$ = 1080 cm^{-1}). This leads to the conclusion that when propionic acid is adsorbed on ZrO_2, the C=O vibrations at $\tilde{\nu}$ = 1800 and 1700 cm^{-1} and the C–O vibration at $\tilde{\nu}$ = 1150 cm^{-1} in free propionic acid disappear due to the formation of a surface-bound carboxylate (see Table 7 a).

© 2014 Wiley-VCH Verlag GmbH & Co. KGaA, Weinheim

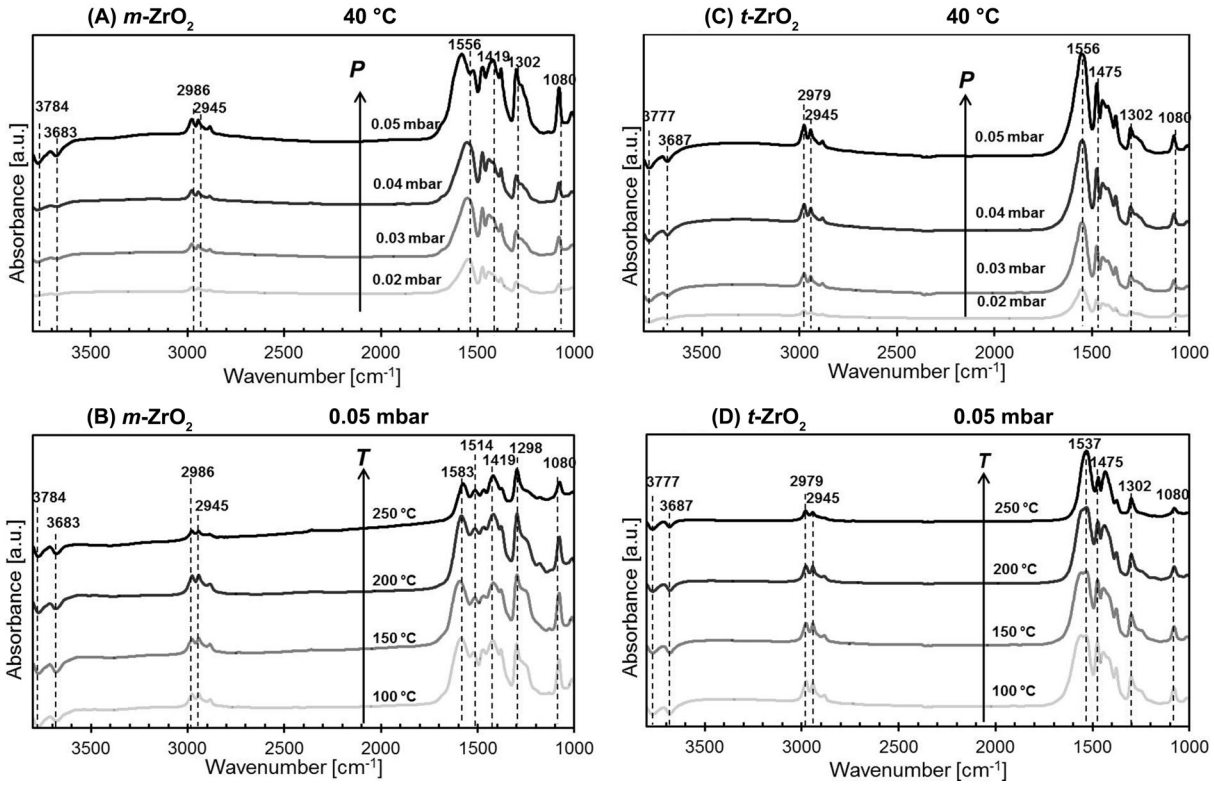

Figure 10. A) and C) IR spectra of adsorbed propionic acid on m-ZrO_2 and t-ZrO_2 with increasing pressures from 0.02 to 0.05 mbar at 40 °C. B) and D) IR spectra of adsorbed propionic acid on m-ZrO_2 and t-ZrO_2 with increasing temperatures from 100 °C to 250 °C at 0.05 mbar pressure.

Figure 10 shows the IR spectra of propionic acid adsorbed on m-ZrO_2 and t-ZrO_2 at partial pressures of 0.02–0.05 mbar and temperatures of 100–250 °C. The spectra are obtained by subtracting the activated ZrO_2 sample. With increasing pressure of propionic acid at 40 °C, the intensity of the characteristic bands on m-ZrO_2 (ν_a, ν_s, ν_{C-H}, δ-CH_3, ρ-CH_3) increased (see Figure 10A), whereas the intensity of the ZrO–H vibration decreased. The concentration of the Zr–OH groups on the surface decreased as the acid is adsorbed on the ZrO_2 surface. At the highest dosing pressure of 0.05 mbar, the peak at $\tilde{\nu}=$ 1556 cm^{-1} of propionic acid was split into two bands at $\tilde{\nu}=$ 1583 and 1525 cm^{-1}. This suggests that propionate partially adsorbs in a monodentate configuration (Table 7B), which is characterized by a much larger splitting of the ν_a(COO) and ν_s(COO) carboxylate stretching frequencies.[15] These adsorbed molecules are competing for the active sites of ZrO_2, monodentate dominates over bidentate at high pressures due to its lower space requirement. Near the reaction temperature of 250 °C (see Figure 10B), only ν_a(COO) and ν_s(COO) decreased markedly in intensity. At the elevated temperatures more molecules were desorbed, lessening the surface coverage and competition by carboxylic acid for the actives sites (i.e., oxygen vacancies). Accordingly, the splitting/difference of the symmetric and asymmetric carboxylate stretching frequencies decreased, which is consistent with the bidentate configuration being dominant over the monodentate one. For propionic acid adsorbing on t-ZrO_2, principally the same species and vibration bands were observed. On increasing the pressure of propionic acid to 0.05 mbar at 40 °C (see Figure 10C), the intensity of the characteristic bands increased, indicating an increasing amounts of adsorbed molecules. Increasing the temperature caused the concentration of adsorbate to decrease (see Figure 10D).

The Ni/m-ZrO_2 and Ni/t-ZrO_2 catalysts showed the same trend upon adsorption of propionic acid as the bare supports, but the concentrations of adsorbed propionic acid was lower (see Figures S7a–d in the Supporting Information). This is consistent with observations that the lower BET surface areas as well as the concentrations of acid sites for Ni/ZrO_2 are lower in comparison to the bare ZrO_2 supports. The concentration of propionic acid adsorbed on the ZrO_2 and Ni/ZrO_2 catalyst surface was quantified through the peak area at $\tilde{\nu}=1080$ cm^{-1} ($\rho(CH_3)$). As shown in Figure 11, the coverage of propionic acid was generally much higher for the bare ZrO_2 supports than for the Ni/ZrO_2 samples. The adsorbed amount increased linearly as a function of the partial pressure of propionic acid from 0.02 to 0.05 mbar (Figure 11A). The results also suggest that m-ZrO_2 adsorbed 1.5 times more propionic acid than t-ZrO_2 at 0.05 mbar and 40 °C, which in both cases expectedly decreased exponentially with temperature (Figure 11B). The amount of propionic acid adsorbed on m-ZrO_2 and Ni/m-ZrO_2 was always more than that on t-ZrO_2 and Ni/t-ZrO_2, respectively. Due to this higher coverage and surface concentration, m-ZrO_2 is concluded to be the more active support for converting stearic acid, because the reaction order is positive in the reactant concentration. This is in good agreement with the experimental

© 2014 Wiley-VCH Verlag GmbH & Co. KGaA, Weinheim

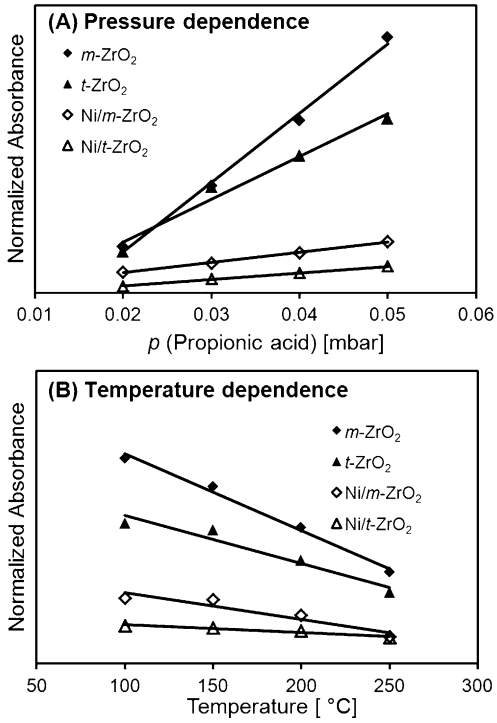

Figure 11. Adsorption of propionic acid on m-ZrO_2, t-ZrO_2, Ni/m-ZrO_2, and Ni/t-ZrO_2 as a function of A) the partial pressure and B) the temperature determined by IR spectroscopy, shown as specific amount (peak area at $\tilde{\nu} = 1080\ cm^{-1}$) normalized by specimen mass.

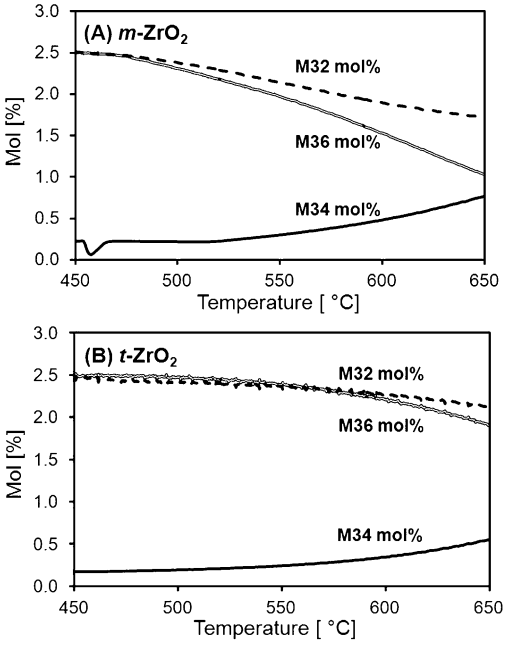

Figure 12. Temperature-programmed isotopic exchange of ^{18}O–^{16}O with A) m-ZrO_2 and B) t-ZrO_2. Mol% of M32 ($^{16}O_2$), M34 (^{18}O–^{16}O), and M36 ($^{18}O_2$) as a function of temperature from 450 to 650 °C with a temperature increase interval of 5 °C min^{-1}.

results above showing m-ZrO_2 to have the higher activity than t-ZrO_2.

Temperature-programmed isotopic exchange (^{16}O–^{18}O) of m- and t-ZrO_2

Figure 12 shows the temperature-programmed isotopic exchange (TPIE) profiles for m-ZrO_2 and t-ZrO_2, respectively, where the mol% of $^{16}O_2$ (M32), ^{18}O–^{16}O (M34), and $^{18}O_2$ (M36) are presented as a function of the temperature. The signal of $^{18}O_2$ with m-ZrO_2 (Figure 12A) decreased from 2.5 to 1.0 mol%. This conversion on m-ZrO_2 is obviously much faster compared to t-ZrO_2 (Figure 12B), which showed a small decrease of the $^{18}O_2$ signal from 2.5–2.0 mol%. Consistent with this, the concentration of ^{18}O–^{16}O increased much faster with m-ZrO_2. The consumption and exchange of $^{18}O_2$ (M36) at m-ZrO_2 ($\Delta =$ 1.5 mol%) was three times higher than on t-ZrO_2 ($\Delta =$ 0.5 mol%), which parallels the difference in the rates the conversion of stearic acid on Ni/m-ZrO_2 and on Ni/t-ZrO_2. In summary, m-ZrO_2 shows a higher activity towards $^{18}O_2$ exchange due to its higher concentrations of defect sites.[16] Therefore, carboxylic acid adsorbs at the exchange sites of the catalyst to a much higher extent, as shown by IR spectroscopy, hence, leading to a higher reactivity in the reduction of stearic acid.

Conclusion

The ZrO_2 morphology of the m-, t-, and mix-ZrO_2 phases affects markedly the hydrodeoxygenation of stearic acid over Ni/ZrO_2 (with identical Ni particle sizes and distribution, as well as BET surface areas and acid and base site concentration) in dodecane. Ni/m-ZrO_2 has a three times higher activity towards stearic acid hydrogenation than Ni/t-ZrO_2 both selectively forming 1-octadecanol at low conversions. Surprisingly, this ratio agrees well with the ratio found for hydrogenation on bare m- and t-ZrO_2. Rate constants for the Ni/ZrO_2-catalyzed hydrogenation reactions of stearic acid are comparable in the fitted and calculated individual measurements indicating very similar adsorption constants for the reactants, the intermediates, and the products. The much lower (fitted) rate constant for the decarbonylation of 1-octadecanol in the overall hydrogenation of stearic acid, is attributed primarily to the competition of the reactants and the intermediates for sites in the conversion. The positive effect of m-ZrO_2 is concluded to be related to the substantially higher adsorbed concentration of the acid (concluded from the higher concentration of adsorbed propionic acid) on m-ZrO_2 compared to t-ZrO_2. The higher concentration of adsorbed reactants is related to the higher concentration of defect sites on the ZrO_2 surface as detected by the higher oxygen exchange ability of the m-ZrO_2 support (quantified in a temperature-programmed isotope exchange experiment). The results show that it is possible to enhance the reactivity for the reductive conversion of fatty acids by maximizing the concentration of oxygen defects sites.

Experimental Section

Chemicals: All chemicals, that is, $Zr(OH)_4 \cdot H_2O$ (XZO 1247/01, MEL Chemicals), $ZrO(NO_3)_2 \cdot H_2O$ (Sigma–Aldrich, 99%), methanol

© 2014 Wiley-VCH Verlag GmbH & Co. KGaA, Weinheim

(Sigma–Aldrich, 99%), urea (Grünning, 99.5%), $Ni(NO_3)_2{\cdot}6H_2O$ (Acros Organics, $\geq$98.5%), stearic acid (Sigma–Aldrich, $\geq$99.5% analytical standard), 1-octadecanol (Sigma–Aldrich, $\geq$99.5% Selectophore), octadecane (Sigma–Aldrich, 99%), heptadecane (Sigma–Aldrich, 99%), dodecane (Sigma–Aldrich, $\geq$99%, ReagentPlus), propionic acid (Sigma–Aldrich, ACS grade $\geq$99.5%) were purchased commercially and were not further purified.

Catalyst preparation: Three types of ZrO_2 supports were synthesized. Mix-phase ZrO_2 was prepared by calcination of $Zr(OH)_4{\cdot}H_2O$ at 400 °C in ambient air for 4 h. Monoclinic and tetragonal ZrO_2 were prepared by the solvothermal method by mixing $ZrO(NO_3)_2$ with water and methanol, respectively.[17] An aqueous or methanolic solution of $ZrO(NO_3)_2$ (0.6 mol L^{-1}) was added with urea (urea/Zr = 10:1). The solvothermal reaction was performed in a stainless-steel autoclave with a Teflon liner at 160 °C and autogenous pressure for 21 h. After washing five times the precipitate with H_2O or MeOH, it was dried over night at 110 °C and then ground and calcined in air at 400 °C for 4 h at a heating rate of 2 °C min^{-1} (flow rate: 100 mL min^{-1}).

The 10 wt% Ni/ZrO_2 catalysts were prepared by impregnation. $Ni(NO_3)_2{\cdot}6H_2O$ (3.30 g) was dissolved in deionized H_2O (5.0 g), and the resulting solution was added dropwise to the support under stirring in ambient air. The slurry was further stirred for 4 h, followed by drying at 110 °C overnight. Subsequently, the ground solid was calcined in synthetic air (flow rate: 100 mL min^{-1}) at 450 °C for 4 h (heating rate: 2 °C min^{-1}) and reduced in a H_2 flow (flow rate: 100 mL min^{-1}) at 500 °C for 4 h (heating rate: 2 °C min^{-1}).

Catalyst characterization: X-ray powder diffraction (XRD) was performed on Philips X'Pert Pro System equipped with a $Cu_{K\alpha}$ radiation source (40 kV, 45 mA) with 1.08° min^{-1} in the 2θ range of 5–70°. The ratio of monoclinic and tetragonal phases in *mix*-ZrO_2 was determined by using Equation (6) with the integrated intensities of the (111) and ($11\bar{1}$) reflecting monoclinic and tetragonal XRD patterns, respectively.[18] The $(111)_m$ and $(11\bar{1})_m$ reflections for the monoclinic phase are at 2θ of 31.4 and 28.3°, respectively, whereas the $(111)_t$ reflection from the tetragonal phase is at 2θ of 30.4°. Accordingly, the actual ratio of monoclinic to tetragonal ZrO_2 in the physically mixed $Ni/(m\text{-}ZrO_2/t\text{-}ZrO_2)$ was determined by using Equation (6) after fitting and integrating the corresponding peaks from the XRD (Figures S1 B and S2 in the Supporting Information).

$$x_m = \frac{I(11\bar{1})_m + I(111)_m}{I(11\bar{1})_m + I(111)_m + I(111)_t} \quad (6)$$

Atomic absorption spectroscopy (AAS) was used to determine the Ni content of the catalysts with a UNICAM 939 AA spectrometer. Prior to measurements, the samples were dissolved in boiling concentrated hydrofluoric acid.

The BET surface area was determined by adsorption–desorption with nitrogen at −196 °C by using a Sorptiomatic 1990 series instrument. The samples were activated in vacuum at 250 °C for 2 h before measurements.

he EDX mappings were obtained by using a JEM-ARM200CF operated at 200 KV with an integrated probe aberration (Cs) corrector and a cold-field emission gun (CFEG) electron source After reduction the finely ground-powdered catalyst samples were stored and mounted under an Ar atmosphere.

Temperature-programmed desorption (TPD) of ammonia and carbon dioxide was carried out in a six-fold parallel reactor system. The pressed samples (500–710 μm) were firstly activated in a He flow at 500 °C for 1 h and loaded with the adsorbent NH_3 or CO_2 at a partial pressure of 1 mbar and 100 °C or 40 °C, respectively. The samples were then purged with He for 1 h in order to remove physisorbed species. After activation, the six samples were heated from 100–770 °C with a rate of 10 °C min^{-1} to desorb NH_3 and from 40 to 700 °C to remove CO_2, and the signals were detected by a Balzers QME 200 mass spectrometer.

Temperature-programmed reactions (TPR) with H_2 were performed in a packed bed flow reactor equipped with a mass spectrometer. First, calcined Ni/ZrO_2 catalyst (100 mg, 250–400 μm) was activated in a He flow at 200 °C (heating rate of 10 °C min^{-1}) for 30 min and cooled to ambient temperature. The reduction was carried out from ambient temperature to 800 °C (heating rate: 10 °C min^{-1}) and maintaining 800 °C for 30 min in 10% H_2/He gas mixture (2 mL min^{-1} H_2/18 mL min^{-1} He). The amount of water produced in the reaction was determined by an online mass spectrometer.

IR spectroscopy of adsorbed propionic acid was performed on a Bruker VERTEX 70 spectrometer at a resolution of 2 cm^{-1} with 128 scans in the range of $\tilde{\nu}$ = 400–4000 cm^{-1}. For the measurements, the samples were pressed into self-supporting wafers and mounted in the sample holder. The ZrO_2 samples were activated in vacuum ($p = 10^{-7}$ mbar) at 300 °C for 1 h. The Ni/ZrO_2 catalysts were activated in H_2 at 400 °C for 1 h, and then subsequently outgassed under vacuum ($p = 10^{-7}$ mbar) to remove H_2 while cooling to 40 °C. The adsorption of propionic acid was performed from 0.01 to 0.05 mbar until equilibrium was reached. In addition, the effect of the temperature was investigated by heating the cell stepwise up to 250 °C. The IR spectra of adsorbed propionic acid were obtained by subtracting the activated sample, and then were normalized by the weight of the sample wafer.

The near-edge structure (XANES) and extended X-ray absorption fine-structure (EXAFS) measurements were performed in the transmission mode at the Pacific Northwest Consortium/X-ray Science Division (PNC/XSD) bending-magnet beamline at Sector 20 of the Advanced Photon Source (APS) at Argonne National Laboratory (ANL). Both Ni (8331.5 eV) and Zr (17 995.88 eV) K-edge spectra were acquired. A combination of monochromator detuning (10%) and a harmonic rejection mirror placed upstream of the I_0 detector reduced contributions from higher harmonics. A Ni or Zr foil was placed downstream of the sample cell as a reference to calibrate the photon energy of each spectrum. Typically, two 15 min scans (Ni edge spectra) and four 15 min scans (Zr edge spectra) were averaged to generate the spectra. The catalyst samples were ground and mixed with boron nitride (catalyst/boron nitride, 20:80 or 5:95 wt% for Ni and Zr edges, respectively), then pressed into 5×12 mm pellets (80 mg) and mounted onto a multiple sample holder. The ATHENA software package[19] was used to remove the background from the $\chi(k)$ oscillations. The Fourier transform of the *k*-space EXAFS data (both real and imaginary parts of $\chi(R)$) were fitted to a theoretical model (FEFF9) calculated by using the ARTEMIS software package. A starting point for evaluating the nanoparticle structure was the measurement of reference standards including bulk (fcc) NiO, bulk (hcp) α-$Ni(OH)_2$, and bulk (fcc) Ni by using literature values for their lattice parameters.[20] A combination of different single and multiple photoelectron scattering paths were used to fit the first five shells of the NiO, α-$Ni(OH)_2$, and Ni nanoparticles.[21] For samples containing both oxidation states, the structural parameters were constrained and then the percentage of each phase was fitted. As a starting point for modeling the ZrO_2 nanoparticles, crystalline *m*-ZrO_2 and bulk *t*-ZrO_2 structures derived from their lattice parameters were used.[22] Single-scattering paths of Zr and O for the monoclinic and tetragonal phase were fitted according to Rush et al.[23]

For the temperature-programmed isotope ($^{18}O_2$–$^{16}O_2$) exchange of *m*- and *t*-ZrO_2, the pelletized supports (100 mg, 500–710 μm) were

© 2014 Wiley-VCH Verlag GmbH & Co. KGaA, Weinheim

diluted in SiC (300 mg) and packed into a fixed-bed reactor (inner diameter 4 mm). After outgassing the samples for 2 h at 450 °C in a He flow (10 mL min^{-1}) $^{18}O_2$ and $^{16}O_2$ were fed simultaneously (each 2.5 mol%) while increasing the temperature to 650 °C (5 °C min^{-1}). The atomic mass units of 32 ($^{16}O_2$), 34 ($^{18}O^{16}O$), and 36 ($^{18}O_2$) in the product stream were recorded as a function of time by a Pfeiffer OmniStarTM GSD 320 OC mass spectrometer.

Measurement of the catalytic activity: For a typical experiment to convert stearic acid or 1-octadecanol, the reactants (1.0 g) and a catalyst (0.1 g) were mixed with dodecane (100 mL), loaded into the reactor (Parr, 300 mL), and then purged three times with H_2. The reaction was carried out at 260 °C in presence of 40 bar H_2 for 2 h at a stirring speed of 600 rpm. In-situ sampling was performed every 20 min, and the liquid samples were analyzed by a Shimadzu 2010 GC-MS by using a HP-5 capillary column (30 m, 0.32 mm inner diameter, 0.25 μm film) equipped with a flame ionization detector (FID). Reproducibility of the rates has been better than ±5% for all experiments.

Acknowledgement

Financial support for S.F., E.B., and C.Z. in the framework of AIgenFlugKraft project of the Bavarian Ministry of Economic Affairs and Media, Energy and Technology (Bayerisches Staatsministerium für Wirtschaft und Medien, Energie und Technologie) and of the Bavarian State Ministry of Education, Science and the Arts (Bayerisches Staatsministerium für Bildung und Kultus, Wissenschaft und Kunst) is highly appreciated. Support of P.X. to take TEM images was provided by the United States (US) Department of Energy (DOE) Grant No. DE-FG02-03ER46057 through the University of California at Davis. Use of TEM was supported under the Laboratory Directed Research and Development Program: Chemical Imaging Initiative at Pacific Northwest National Laboratory (PNNL), a multi-program national laboratory operated for DOE by Battelle under Contract DE-AC05-76L01830. TEM was performed at EMSL, a DOE Office of Science user facility sponsored by the Office of Biological and Environmental Research and located at PNNL. XAFS measurements and related work performed by J.L.F., Z.A.C., and D.M.C. were supported by the US DOE Office of Science, the Office of Basic Energy Sciences (BES), the Division of Chemical Sciences, Geosciences & Biosciences. PNC/XSD facilities at the Advanced Photon Source (APS), and research at these facilities, are supported by DOE/BES, the Canadian Light Source and its funding partners, the University of Washington, and the APS. Use of the APS, an Office of Science User Facility operated for the DOE Office of Science by Argonne National Laboratory, was supported by the DOE under Contract No. DE- AC02-06CH11357. The assistance of Dr. Nigel Browning (PNNL) in performing TEM and Dr. Mahalingam Balasubramanian (APS) in performing XAFS measurements is highly appreciated. We thank Franz-Xaver Hecht for N_2-sorption and Martin Neukamm for AAS measurements, and gratefully acknowledge help provided by Robin Kolvenbach for kinetic fitting, and Christian A. Gärtner for isotopic exchange (^{16}O–^{18}O) experiments.

Keywords: decarbonylation · EDX-TEM · hydrodeoxygenation · IR spectroscopy · isotopes · XAFS

[1] G. W. Huber, S. Iborra, A. Corma, *Chem. Rev.* **2006**, *106*, 4044 – 4098.
[2] J. Jakkula, V. Niemi, J. Nikkonen, V.-M. Purola, J. Myllyoja, P. Aalto, J. Lehtonen, V. Alopaeus, Process for producing a hydrocarbon component of biological origin, Fortum Oyj, Finland, Neste Oil Oyj., **2004**, p. 12.
[3] a) C. Zhao, T. Bruck, J. A. Lercher, *Green Chem.* **2013**, *15*, 1720 – 1739; b) E. Furimsky, *Catal. Rev.* **1983**, *25*, 421 – 458.
[4] a) B. Peng, X. Yuan, C. Zhao, J. A. Lercher, *J. Am. Chem. Soc.* **2012**, *134*, 9400 – 9405; b) B. Peng, Y. Yao, C. Zhao, J. A. Lercher, *Angew. Chem. Int. Ed.* **2012**, *51*, 2072 – 2075; *Angew. Chem.* **2012**, *124*, 2114 – 2117.
[5] B. Peng, C. Zhao, S. Kasakov, S. Foraita, J. A. Lercher, *Chem. Eur. J.* **2013**, *19*, 4732 – 4741.
[6] a) M. D. Rhodes, A. T. Bell, *J. Catal.* **2005**, *233*, 198 – 209; b) M. D. Rhodes, K. A. Pokrovski, A. T. Bell, *J. Catal.* **2005**, *233*, 210 – 220.
[7] a) B.-Q. Xu, J.-M. Wei, Y.-T. Yu, J.-L. Li, Q.-M. Zhu, *Top. Catal.* **2003**, *22*, 77 – 85; b) E. Tani, M. Yoshimura, S. Somiya, *J. Am. Ceram. Soc.* **1983**, *66*, 11 – 14.
[8] C. Zhao, Y. Yu, A. Jentys, J. A. Lercher, *Appl. Catal. B* **2013**, *132 – 133*, 282 – 292.
[9] a) K. Hadjiivanov, M. Mihaylov, D. Klissurski, P. Stefanov, N. Abadjieva, E. Vassileva, L. Mintchev, *J. Catal.* **1999**, *185*, 314 – 323; b) W. Song, C. Zhao, J. A. Lercher, *Chem. Eur. J.* **2013**, *19*, 9833 – 9842.
[10] a) E. Chenu, G. Jacobs, A. C. Crawford, R. A. Keogh, P. M. Patterson, D. E. Sparks, B. H. Davis, *Appl. Catal. B* **2005**, *59*, 45 – 56; b) P. Li, I. W. Chen, J. E. Penner-Hahn, *Phys. Rev. B* **1993**, *48*, 10063 – 10073.
[11] a) Y. L. Soo, P. J. Chen, S. H. Huang, T. J. Shiu, T. Y. Tsai, Y. H. Chow, Y. C. Lin, S. C. Weng, S. L. Chang, G. Wang, C. L. Cheung, R. F. Sabirianov, W. N. Mei, F. Namavar, H. Haider, K. L. Garvin, J. F. Lee, H. Y. Lee, P. P. Chu, *J. Appl. Phys.* **2008**, *104*, 113535 – 113535; b) L. M. Acuña, D. G. Lamas, R. O. Fuentes, I. O. Fábregas, M. C. A. Fantini, A. F. Craievich, R. J. Prado, *J. Appl. Crystallogr.* **2010**, *43*, 227 – 236; c) P. Yang, X. Cai, Y. Xie, Y. Xie, T. Hu, J. Zhang, T. Liu, *J. Phys. Chem. B* **2003**, *107*, 6511 – 6513.
[12] N. Thromat, C. Noguera, M. Gautier, F. Jollet, J. P. Duraud, *Phys. Rev. B* **1991**, *44*, 7904 – 7911.
[13] a) R. Pestman, R. M. Koster, E. Boellaard, A. M. van der Kraan, V. Ponec, *J. Catal.* **1998**, *174*, 142 – 152; b) R. Pestman, R. M. Koster, J. A. Z. Pieterse, V. Ponec, *J. Catal.* **1997**, *168*, 255 – 264; c) R. Pestman, R. M. Koster, A. van Duijne, J. A. Z. Pieterse, V. Ponec, *J. Catal.* **1997**, *168*, 265 – 272; d) R. Pestman, A. van Duijne, J. A. Z. Pieterse, V. Ponec, *J. Mol. Catal. A: Chem.* **1995**, *103*, 175 – 180.
[14] a) Z. F. Pei, V. Ponec, *Appl. Surf. Sci.* **1996**, *103*, 171 – 182; b) K. H. Jacob, E. Knoezinger, S. Benier, *J. Mater. Chem.* **1993**, *3*, 651 – 657.
[15] a) L. Chen, Y. Zhu, H. Zheng, C. Zhang, Y. Li, *Appl. Catal. A* **2012**, *411 – 412*, 95 – 104; b) W. Rachmady, M. A. Vannice, *J. Catal.* **2002**, *207*, 317 – 330.
[16] E. Heracleous, A. A. Lemonidou, *J. Catal.* **2006**, *237*, 175 – 189.
[17] W. Li, H. Huang, H. Li, W. Zhang, H. Liu, *Langmuir* **2008**, *24*, 8358 – 8366.
[18] H. K. Schmid, *J. Am. Ceram. Soc.* **1987**, *70*, 367 – 376.
[19] B. Ravel, M. Newville, *J. Synchrotron Radiat.* **2005**, *12*, 537 – 541.
[20] a) N. Smith, *J. Am. Chem. Soc.* **1936**, *58*, 173 – 179; b) H. Bode, K. Dehmelt, J. Witte, *Electrochim. Acta* **1966**, *11*, 1079 – 1087.
[21] A. I. Frenkel, C. W. Hills, R. G. Nuzzo, *J. Phys. Chem. B* **2001**, *105*, 12689 – 12703.
[22] a) F. J. Torres, J. M. Amigó, J. Alarcón, *J. Solid State Chem.* **2003**, *173*, 40 – 44; b) W. W. Barker, F. P. Bailey, W. Garrett, *J. Solid State Chem.* **1973**, *7*, 448 – 453.
[23] G. E. Rush, A. V. Chadwick, I. Kosacki, H. U. Anderson, *J. Phys. Chem. B* **2000**, *104*, 9597 – 9606.

Received: September 17, 2014
Published online on ■■ ■■, 0000

© 2014 Wiley-VCH Verlag GmbH & Co. KGaA, Weinheim

FULL PAPER

Finding the best: Three different Ni/ZrO_2 catalysts have been tested with regard to their efficiency in the hydrogenation reaction of stearic acid. The Ni/*m*-ZrO_2 catalyst was found to be the best one. A higher concentration of active oxygen defects present in this combination was identified to be responsible for the superiority of this catalyst over the other systems (see scheme).

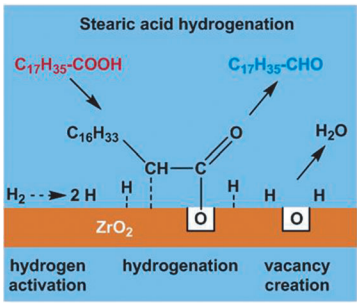

Microalgae Oil

*S. Foraita, J. L. Fulton, Z. A. Chase, A. Vjunov, P. Xu, E. Baráth, D. M. Camaioni, C. Zhao, J. A. Lercher**

■■ – ■■

Impact of the Oxygen Defects and the Hydrogen Concentration on the Surface of Tetragonal and Monoclinic ZrO_2 on the Reduction Rates of Stearic Acid on Ni/ZrO_2

© 2014 Wiley-VCH Verlag GmbH & Co. KGaA, Weinheim